Impact of the Mutation A21G (Flemish Variant) on Alzheimer's β-Amyloid Dimers by Molecular Dynamics Simulations

Alexis Huet and Philippe Derreumaux
Laboratoire de Biochimie Théorique, UPR 9080, Centre National de la Recherche Scientifique, Institut de Biologie Physico-Chimique, et Université Paris, Paris, France

ABSTRACT Soluble oligomers of the amyloid β-protein (Aβ) are linked to Alzheimer's disease. Irrespective of the nature of the nucleus before fibril growth, dimers are essential species in Aβ assembly, but their transient character has precluded, thus far, high-resolution structure determination. We have investigated the effects of the point mutation A21G on Aβ dimers by performing high temperature all-atom molecular dynamics simulations of $A\beta_{40}$, $A\beta_{42}$, and their Flemish variants (A21G) starting from their fibrillar conformations. Aβ dimers are found in equilibrium between various topologies, and the absence of common structural features shared by the four species makes problematic the design of a unique inhibitor for blocking dimers. We also show that the impact of the point mutation A21G on Aβ structure and dynamics varies from $A\beta_{40}$ to $A\beta_{42}$. Finally, we provide a possible structural explanation for the reduced aggregation rate of Aβ fibrils containing the Flemish disease-causing mutation.

INTRODUCTION

The formation of amyloid fibrils is a hallmark of many human diseases and results from the misfolding of proteins into cross β-sheet structure (1). Alzheimer's disease, for instance, is characterized by deposition of amyloid fibrils in the brain parenchyma and cortical blood vessels. This accumulation consists of 40- and 42-mer peptides ($A\beta_{40}$ and $A\beta_{42}$) produced through endoproteolysis of the β-amyloid precursor transmembrane protein by β- and γ-protease (2). Thus far, a high-resolution structure for $A\beta_{40}$ and $A\beta_{42}$ is not available, in contrast to a seven-residue peptide fragment from yeast protein Sup35 (3), but we know that the β-strands run perpendicular to the fiber axis, the hydrogen-bonding interactions run parallel to the fiber axis, and the chains are in parallel register. Several models have been proposed, based on solid-state NMR experiments (4,5), hydrogen/deuterium (H/D) exchanges measurements with (6) or without mutagenesis data (7), and proline scanning methods (8,9). All models share a disordered N-terminal region spanning at least residues 1–10, and differ in the number and length of strands and loops, and in the network of intermolecular hydrogen-bonding and sidechain-sidechain interactions.

The kinetic model, by which the Aβ peptides aggregate into amyloid fibrils, is believed to follow a nucleation-growth model, with a lag-phase of several days. Oligomerization is very sensitive to amino-acid variations. Residues 41 and 42 affect the characteristics of the nucleus (10); $A\beta_{42}$ forms fibrils at a higher rate than $A\beta_{40}$ and the Alzheimer's disease-causing A21G (Flemish) mutation (11) has a slower aggregation kinetic than wild-type Aβ and the E22Q (Dutch) (12,13), E22K (Italian) (14), E22G (Arctic) (15), and D23N (Iowa) (16) mutations (17,18).

In contrast to the late aggregates or protofibrils which are well characterized, the structures of the oligomers forming in the early steps of aggregation are poorly understood because they are transient in character. Although dimers are in equilibrium with higher-order species before the formation of the nucleus, dimer formation is certainly critical in Aβ assembly. However, much remains to be elucidated regarding the structure of these dimers, which are sufficient for toxicity (19,20), from both the experimental and theoretical fronts. We know, however, that $A\beta_{40}$ and $A\beta_{42}$ form stable dimers in solution using fluorescence resonance energy transfer (21–23). The stability of several Aβ species in dimers and higher-order mers has been investigated by explicit solvent molecular dynamics (MD) simulations, including dimers of $A\beta_{10-35}$ (24), hexamers of $A\beta_{15-36}$ (25,26), and octamers of $A\beta_{9-40}$ (27). These studies at 300 K, however, explore local fluctuations around preformed arrangements. The assembly process of $A\beta_{1-40}$ and $A\beta_{1-42}$ dimers was studied by discontinuous MD (DMD) simulations, and planar β-strand Aβ dimers were found instable (28). Similarly, the aggregation process of multimers of $A\beta_{40}$ and $A\beta_{42}$ (29) has been explored using DMD simulations, but the results remain to be confirmed using a more elaborated chain representation and force field (29).

In this study, we have investigated the effects of the point mutation A21G on Aβ dimers by performing all-atom molecular dynamics simulations of $A\beta_{9-40}$, $A\beta_{9-42}$ and their Flemish variants (A21G) at 400 K starting from their fibrillar conformations. Note that omission of residues 1–8 does not prevent the peptide from forming fibrils (30). The point mutation A21G is interesting because no mechanistic explanation has been offered for its effect on aggregation rate, in contrast to the mutations at positions 22 and 23 (31,32). We emphasize that our goal is not to determine the equilibrium structures of Aβ dimers. This is currently out of reach by

Submitted June 8, 2006, and accepted for publication July 19, 2006.

Address reprint requests to P. Derreumaux, Tel.: 33-1-58-41-50-16; E-mail: philippe.derreumaux@ibpc.fr.

0006-3495/06/11/3829/12 $2.00

doi: 10.1529/biophysj.106.090993

using high temperature MD simulations or replica exchange simulations with current computer facilities. Rather, our aim is to understand at an atomic level of detail the effects of the mutation A21G on fibrillarlike dimeric structures of Aβ_{40} and Aβ_{42}.

MATERIALS AND METHODS

Differences in Aβ_{40} and Aβ_{42} fibril models

The Aβ_{42} sequence is

DAEFRHDSGYEVHHQKLVFF*A*
EDVGSNKGAIIGLMVGGVV**IA**

with the amino acids 21 underlined and 41 and 42 in bold. Several fibril models have been proposed. Both Aβ_{40} models of 2002 (4) and 2006 (5) models of Petkova et al. are based on solid-state NMR measurements, but the 2006 model includes measurements that provide direct constraints on quaternary structure. The 2005 Aβ_{42} model of Luhrs et al. (6) is based on the solid-state NMR measurements carried by Petkova et al. in 2002, and on their own H/D exchange and mutagenesis data. Olofsson et al. (7) have also performed H/D exchange measurements on Aβ_{42} fibrils. All these models show a cross-β structure with parallel β-sheets, but significant differences are identified.

1. Residues 1–8 are disordered in the 2002 and 2006 Aβ_{40} models, versus residues 1–15 in the 2005 Aβ_{42} model proposed by Luhrs et al. (6). As the result, β-strand S1 encompasses residues 12–24 in the Aβ_{40} models versus 18–26 in the Aβ_{42} Luhr's model, and β-strand S2 covers residues 30–40 and 31-42, respectively. In contrast, Olofsson et al. (7) found that residues 11–24 are highly protected in Aβ_{42}, in agreement with the Petkova's Aβ_{40} models, so the two fibril structures may actually be very similar.
2. The salt bridge between residues Asp^{23} and Lys^{28} and the side-chain interactions are intramolecular in the 2002 Aβ_{40} model, but intermolecular in the 2005 Aβ_{42} model. The inter-β-sheet side-chain interactions are between the odd-numbered residues of S1 and S2 in the 2002 Aβ_{40} model, and between the odd-numbered residues of S1 and the even-numbered residues of S2 in the 2005 Aβ_{42} model. However, the revisited 2006 Aβ_{40} model indicates intermolecular Asp^{23}–Lys^{28} salt bridges and contacts between odd residues in S1 with even residues in S2.

These analyses, with the proposed model of Williams et al. (8), indicate that the fibril structures are likely to evolve as additional experimental data become available, but such a refinement is very complicated since the dimensions and morphologies of fibrils vary with solution conditions and degrees of agitation (33).

Dynamics simulations

MD simulations are performed at neutral pH using the program GROMACS2.0 and the all-hydrogen energy function GROMOS96 (34). The starting point is the 2002 NMR solid-state structure of Aβ_{40} fibril (4), which lacks the atomic positions of residues 1–8. Note that both the Aβ_{42} model and the 2006 Aβ_{40} model were unknown at the beginning of this work. The initial structures for Aβ_{42} and the A21G variants are constructed using the SWISS-MODEL server (35).

All Aβ models are solvated in a rectangular box of 90, 50, and 40 Å sides with ~6000 simple point-charge water molecules and simulated using periodic boundary conditions. The particle-mesh Ewald method is used with a cutoff distance of 12 Å. Aβ models are minimized by 300 steps of steepest descent and 600 steps of conjugate gradient and then equilibrated at the desired temperature for 80 ps under Cα atom restraints followed by 80 ps free of any atomic restraints. Subsequently, MD simulations are performed in the canonical NPT ensemble. The time step for dynamics is 2.0 fs using the LINCS algorithm and the list of nonbonded interactions is updated every 20 fs. Temperature is controlled using a weak coupling to a bath of constant T (coupling time of 0.1 ps) and pressure by a weak coupling to a bath of constant P (1 atm, coupling time of 0.5 ps).

All Aβ models are simulated for 10 ns at 400 K to increase phase space sampling. This is an advisable choice in contrast to the standard temperature (500 K) to induce unfolding and conformational changes. The Van Gunsteren group (36) showed that the use of temperatures higher than 400 K is very likely to affect the unfolding, kinetics, and thermodynamics of proteins. Dinner and Karplus (37) studied thermal folding and unfolding of lattice proteins and found that unfolding is the reversal of fast-track folding. Klimov and Thirumalai (38) moved one step further and showed that folding pathways at 300 K and unfolding pathways at 390–420 K are similar using off-lattice models. It follows that the present paths at 400 K are closely related to the conformational changes at 300 K, although the population of each dominant unfolded state changes with T. The Aβ_{40} and its A21G variant are also simulated starting from the same structure using different initial velocities. All runs took 80 days on a cluster of five 1.5-GHz processors.

The trajectories are analyzed using several order parameters. These include the Cα root mean-square (RMS) deviations from the minimized NMR structure and the Cα RMS fluctuations (RMSF) relative to the average MD structure. We also follow the evolution of the radius of gyration R_g, the end-to-end distance, and the percentage of secondary structure content using the STRIDE program (39). Because the Aβ models differ in length, we only use residues 9–40 to compare the trajectories. The MD-generated structures are also clustered using a Cα RMS deviation cutoff of 3 Å, and analyzed by their contact maps and percentages of native contacts. Here, native refers to the 2002 Aβ_{40} solid-state NMR conformation, and a contact is defined when aliphatic carbon atoms of two nonsequential side chains come within 5.4 Å or any other atom of two nonsequential side chains lies within 4.6 Å (40). The structural models are drawn by using the VMD software (41).

RESULTS

Conformational stability of dimers

The distributions of the Cα RMS deviations (RMSDs) of residues 9–40 from the minimized structures of monomers A and B are displayed in Fig. 1, *a* and *b*, for all Aβ models. Aβ_{40} is much less flexible than Aβ_{42} and the mutants. The Cα RMSD population of monomer A is essentially centered at 0.5 nm in Aβ_{40}, and varies between 0.5 and 0.9 nm in Aβ_{42}-A21G, 0.7 and 1.1 nm in Aβ_{42}, and between 0.7 and 1.25 nm in Aβ_{40}-A21G. The variability in conformations can be further explored by the distributions of the end-to-end Cα distances between residues 9 and 40 in Fig. 1, *c* and *d*. In Aβ_{40}, the most populated end-to-end distance is centered at 2 nm in monomer A and spans larger distances in monomer B, which is in contrast with Aβ_{42}, where the end-to-end distance fluctuates between 0.8 and 2.8 nm in both monomers. Higher stability of Aβ_{40} is also seen in the evolution of the radius of gyration (R_g) with time in Fig. 1 *e* and the distributions of R_g in Fig. 1 *f*. In Aβ_{40}, the MD-averaged R_g is 1.5 nm to be compared to the NMR value of 1.75 nm, and the R_g distribution has a well-defined peak. This contrasts with Aβ_{42} and the mutants which have a lower mean radius of gyration (1.1 nm in Aβ_{40}-A21G, Fig. 1 *e*) and larger standard deviations of R_g (Fig. 1 *f*).

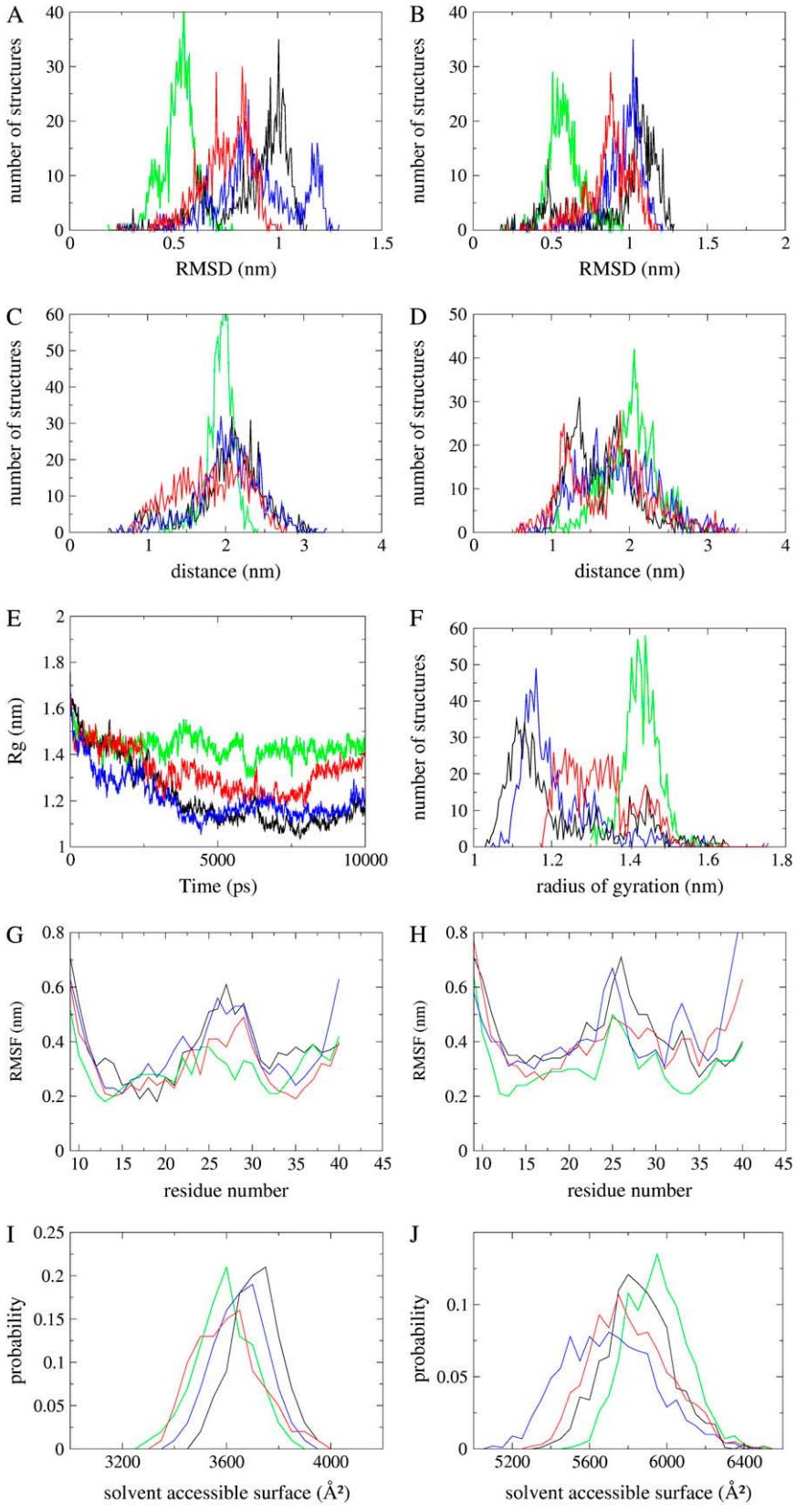

FIGURE 1 Dynamical properties as a function of Aβ species. Distributions of the RMSDs from the minimized structures: (*A*) monomer A and (*B*) monomer B. Distributions of the Cα–Cα distances between residues 9 and 40: (*C*) monomer A and (*D*) monomer B. Radius of gyration as a function of time (*E*) and distributions of the radius of gyration (*F*); both panels use the dimer of each species. RMSFs from their mean structures: (*G*) monomer A and (*H*) monomer B. Distributions of the solvent-exposed surface area: (*I*) main-chain atoms of residues 9–40 and (*J*) side-chain atoms of residues 9–40; both panels use the dimer of each species. Four colors are used to distinguish the species: green ($A\beta_{40}$); blue ($A\beta_{40}$-A21G); black ($A\beta_{42}$); and red ($A\beta_{42}$-A21G).

The RMSFs, with respect to the average MD structure in Fig. 1, *g* and *h*, show high flexibility at the N-terminal and C-terminal extremities for all models, in agreement with MD studies of a dimer of $A\beta_{10-35}$ (24) and eight $A\beta_{40}$ peptides (27). The largest differences in RMSF between all Aβ species are found in the loop between S1 and S2 (residues 21–30, RMSF of 0.3 Å in $A\beta_{40}$ versus 0.6 Å in other species, Fig. 1 *g*), and in strand S2 (notably for monomer B, Fig. 1 *h*). These regions match the locations where experimental data show the lowest structural determination.

The structural fluctuations, using the RMSD from the minimized and MD-averaged structures, the end-to-end distance, and the radius of gyration show that monomer A is less flexible than monomer B. This asymmetry in structural fluctuations of the monomers in a homodimer has been discussed in 10-ns MD simulations on decoys of $A\beta_{10-35}$ at 300 K (24). Asymmetric conformational changes were also observed by lattice (42) and off-lattice (43) aggregation MC simulations of homodimer amyloid-forming models. The effect of this asymmetry on fibril nucleus formation, remains, however, to be determined.

Overall, we see that the flexibility increases in the following order: $A\beta_{40} \rightarrow A\beta_{42}$ A21G $\rightarrow A\beta_{42}$ and $A\beta_{40}$-A21G. This conclusion is also supported by the analysis of the solvent-exposed surface area, using the method of Lee and Richards (44), although the role of water molecules on dimer unfolding changes according to different sequences. The backbone atoms of residues 9–40 are more exposed to the solvent in $A\beta_{42}$ and $A\beta_{40}$-A21G than in $A\beta_{40}$ (Fig. 1 *i*). The side-chain atoms of residues 9–40 are more exposed in $A\beta_{40}$ than in $A\beta_{42}$ and the Aβ variants (Fig. 1 *j*). (Identical results are obtained excluding residue 21.) This change in solvent accessibility does not have a one-to-one mapping with the amino-acid number. For instance, the distributions of solvent accessibility of the Asp^{22} side chain match exactly in all simulations, whereas those of Asp^{11} side-chain change (data not shown).

To investigate whether these results vary with different initial velocity distributions, the simulations of $A\beta_{40}$ and $A\beta_{40}$-A21G are repeated for 10 ns using the same starting structure. The RMSD between all pairs of structures is determined using a pool of 1000 structures taken at 10-ps intervals. By calculating for each Aβ species the number of pairs of structures as a function of the RMSD deviation, we see that the RMSD plots superpose well from one run to another for $A\beta_{40}$ (Fig. 2 *a*) and $A\beta_{40}$-A21G (Fig. 2 *b*). Consistency between the runs is also seen in the Cα RMSD from the minimized structure in Fig. 2 *c* and the evolution of the radius of gyration with time in Fig. 2 *d*. Fig. 2, *e* and *f*, show the RMSF profiles of monomers A and B in $A\beta_{40}$-A21G. The RMSFs are very similar in monomer A, but differ by 2 Å in the 25–32 region of monomer B. Overall, these analyses indicate that different simulations on the same sequence produce equivalent results.

Effects on secondary structures and loop conformations

Table 1 gives the mean percentage and standard deviation of α-helix, β-strand, and turn and random coil contents, using residues 9–40 for all species. As expected from high temperature simulations ignoring interactions with neighboring protofilaments, the percentage of β-strand decreases, but the variation with Aβ length and mutation A21G is rather surprising. Note that the percentage of β-strand is 83% (26:31) in the NMR-model of $A\beta_{9-40}$. The MD-averaged percentage of β-strand is 46% in both $A\beta_{40}$ and $A\beta_{42}$-A21G, and 37% in $A\beta_{40}$-A21G and $A\beta_{42}$. The variation in β-strand content does not result from an increase in α-helix (its population amounts to a few percent) and turn content, but in random coil conformations.

To quantify the effects of extending or mutating $A\beta_{40}$ on secondary structures, we calculate the probability of each residue to be assigned with β-strand character along the trajectories. We see that, in $A\beta_{40}$, the strands S1 and S2 are rather well-conserved spanning residues 11–20 and 30–36 in both monomers (Fig. 3 *a*), whereas in $A\beta_{42}$ and the mutants, monomer B is clearly less β-prone than monomer A, and the details vary from one Aβ species to another. For instance, the reduction of β-content in $A\beta_{40}$-A21G results from a shorter strand S1 in monomer B spanning residues 12–18 (but not monomer A, Fig. 3 *b*), and shorter strands S2 in monomers A and B. In contrast, the reduction of β content in $A\beta_{42}$ comes from a shorter strand S2 in monomer A and broken strands S2 in monomer B (see the minimum at positions 37–38 in Fig. 3 *c*). Finally, the combined impact of A21G and residues 41–42 on β-strand percentage is rather complex: they shorten strand S1 (monomer B) or extend it by four residues (monomer A); they break strand S2 with turn preferences at positions 37–38 (monomer B) or extend it at positions 39–41 (Fig. 3 *d*).

To determine why the mutation A21G destabilizes β-sheets in $A\beta_{40}$ but not in $A\beta_{42}$, in Fig. 4 we plot the Ramachandran plot of the residue 21 from all MD-generated structures of each Aβ model. We see that in $A\beta_{40}$ and $A\beta_{42}$, Ala^{21} explores essentially the favored (ϕ,ψ) regions with a high density of residues with β-character (Fig. 4, *a* and *c*). On the other hand, in $A\beta_{40}$-A21G, the Ramachandran plot of Gly^{21} has a typical pattern of a glycine (Fig. 4 *b*), whereas in $A\beta_{42}$-A21G, the Ramachandran plot resembles that of a standard residue (Fig. 4 *d*). These results indicate that the residues 41 and 42 have a strong impact on the flexibility of the residue Gly at position 21, and may affect the loop-spanning residues 21–30.

To quantify the variations of this loop, we calculate the intramolecular and intermolecular distances between the N^{ζ} atom of Lys^{28} and C^{γ} atom of Glu^{22} and Asp^{23}. Salt bridges are considered formed if they come within 4.2 Å (45). The formation times of all salt-bridges during the trajectories are reported in Table 2. As expected, we find that the native

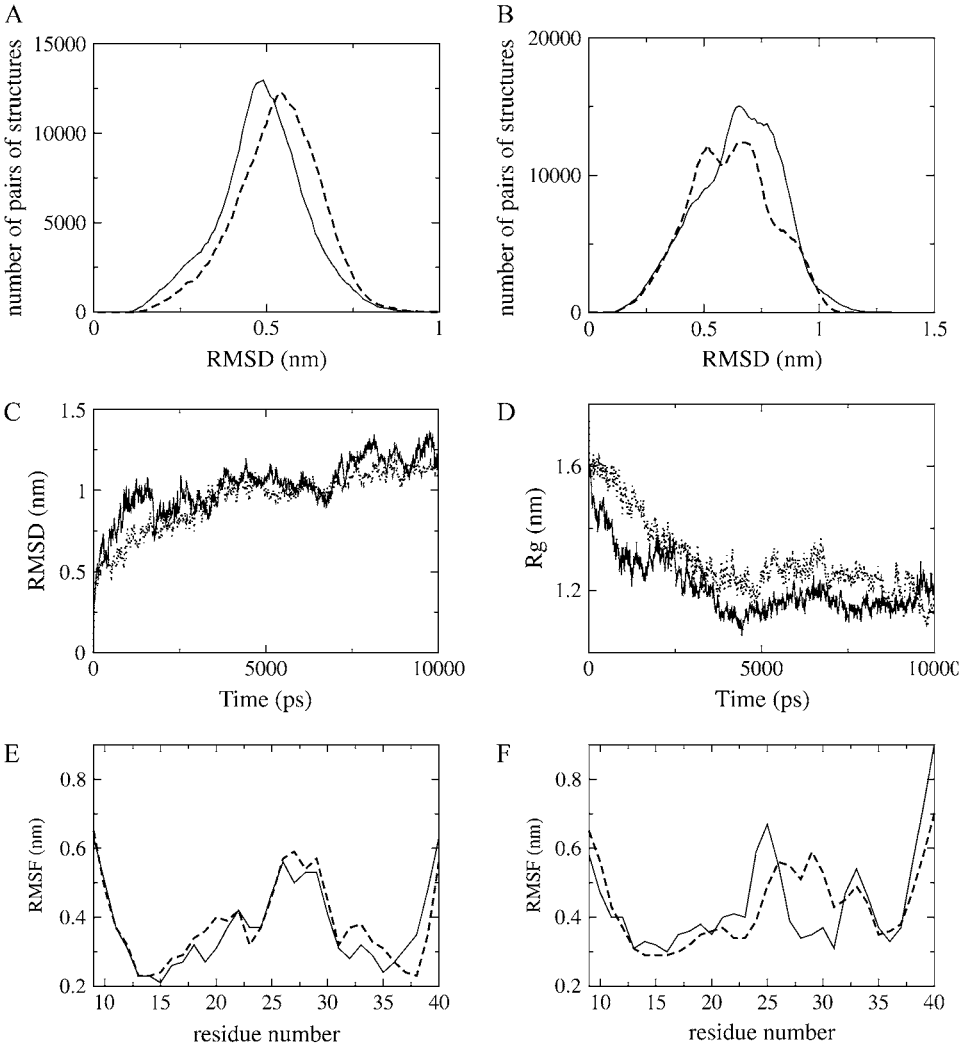

FIGURE 2 Effects of two different initial velocities on $A\beta_{40}$ and $A\beta_{40}$-A21G properties. Number of pairs of structures as a function of the RMSD for $A\beta_{40}$ runs (*A*) and $A\beta_{40}$-A21G runs (*B*). RMSD (*C*) and radius of gyration (*D*) as a function of time for the dimers of Aβ40-A21G. RMSFs from their mean structures for the monomer A (*E*) and the monomer B (*F*) of Aβ40-A21G. Solid lines are used for the first seed and dotted lines for the second seed.

intramolecular Asp^{23}-Lys^{28} salt bridge is populated in all models, although to a lesser extent in $A\beta_{42}$ (34% of the time) compared to $A\beta_{40}$ (52% of the time). Note that A21G reduces the occurrence of this salt bridge: 32% of the time in $A\beta_{40}$-A21G and 22% of the time in $A\beta_{42}$-A21G. Similarly, the nonnative intramolecular Glu^{22}-Lys^{28} salt bridge is also populated in all models: 10.7%, 9.7%, 14.8%, and 15.8% for $A\beta_{40}$, $A\beta_{42}$, $A\beta_{40}$-A21G, and $A\beta_{42}$-A21G, respectively. The finding of two distinct Coulombic interactions involving Lys^{28} are fully consistent with recent NMR experiments of the monomer of the fragment $A\beta_{21-30}$ (31). Interestingly, the intermolecular salt bridge between Asp^{23} of monomer B and Lys^{28} of monomer A, one fingerprint of the 2005 $A\beta_{42}$ model and the 2006 $A\beta_{40}$ model, is also populated in all simulations, and notably in $A\beta_{40}$ (22.6% of the time) and $A\beta_{42}$-A21G (13.4% of the time).

TABLE 1 Secondary structure compositions of $A\beta_{40}$, $A\beta_{42}$ and their A21G variants from explicit solvent MD simulations at 400 K

Protein	Strand	Helix	Turn	Coil
$A\beta_{40}$	46.4 ± 9.8	0.3 ± 1.6	2.2 ± 2.7	51.0 ± 11.3
$A\beta_{40}$-A21G	37.0 ± 14.6	0.6 ± 3.1	7.2 ± 5.8	55.2 ± 12.1
$A\beta_{42}$	37.1 ± 12.5	0.6 ± 2.3	4.2 ± 4.0	58.1 ± 13.5
$A\beta_{42}$-A21G	47.2 ± 11.4	0.6 ± 2.8	3.8 ± 3.7	48.3 ± 13.2

Secondary structure assignment is carried out using the STRIDE program (39). For each protein, we give the mean and standard deviation of secondary structure percentages using only residues 9–40.

Geometrical characteristics of final Aβ dimers

The centers of the most populated clusters within 7.5–10 ns are shown in Fig. 5. The populations of these clusters vary from 40% ($A\beta_{40}$-A21G) to 80% ($A\beta_{42}$-A21G). The side-chain-sidechain contact map of each final topology is given in Fig. 6.

As a result of unfolding, the percentage of native sidechain-sidechain contacts averages 40% in $A\beta_{40}$, 22% in Aβ42, 20% in $A\beta_{42}$-A21G, and 19% in $A\beta_{40}$-A21G, and all final structures adopt nonnative topologies, as described

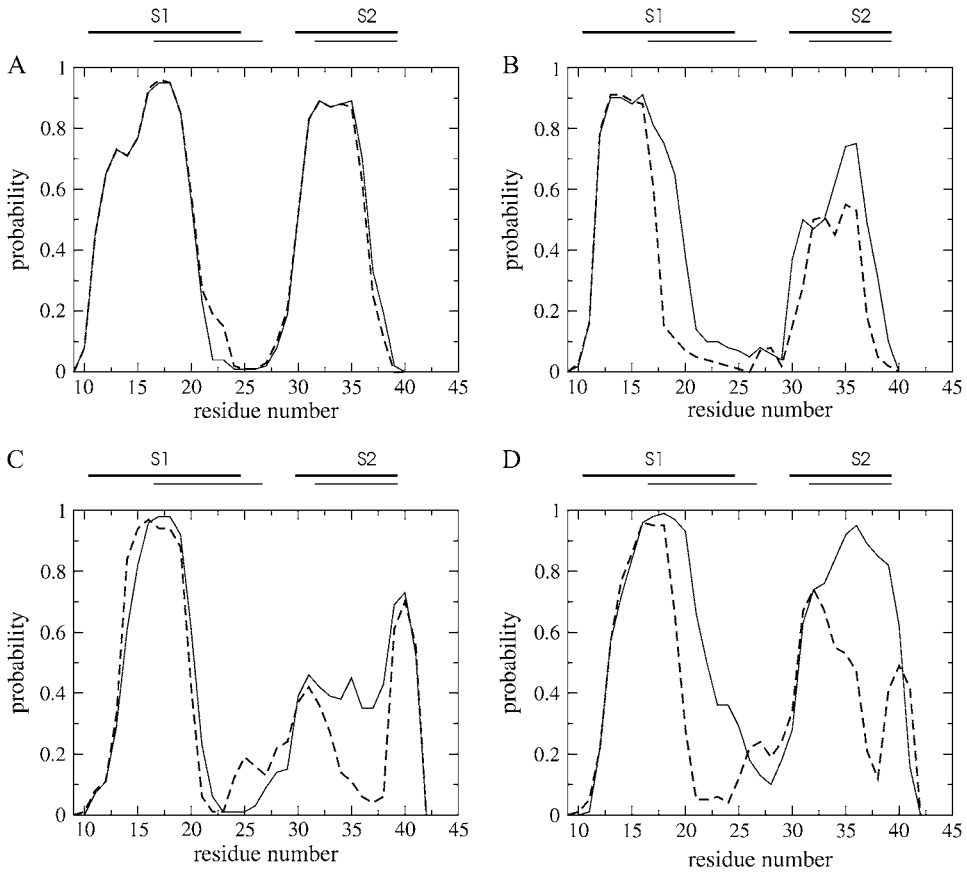

FIGURE 3 MD-averaged probability of β-strand occurrence along the amino-acid sequence. Aβ_{40} (*A*), Aβ_{40}-A21G (*B*), Aβ_{42} (*C*), and Aβ_{42}-A21G (*D*). The location of the β-strands S1 and S2 within the 2002 Aβ_{9-40} model and the 2005 Aβ_{17-42} model are indicated by thick and thin solid lines, respectively. In each panel, solid lines are used for the monomer A and dotted lines for the monomer B.

by TOPS cartoons (46). In what follows, we analyze, for each Aβ species, the topological reorganization, the salt bridge within the (21–30) loop, and the intra- and intermolecular interactions involving notably Met^{35}, Phe^{19}, Phe^{20}, Ile^{41}, and Ala^{42} (5). We recall that, in the starting Aβ_{40} structure shown in Fig. 5 *a*, residues *i* of monomer A are in contact with residues *i* of monomer B, both intramolecular and intermolecular contacts are formed between Phe^{19} and Met^{35}, and between His^{13} and Ile^{41} (Fig. 6 *a*, panel *AB*).

The final topology of Aβ_{40} in Fig. 5 *b* is a planar four-stranded β-sheet with native parallel registers between the strands S1 and between the strands S2, and nonnative antiparallel hydrogen-bonds between S2 of monomer B and S1 of monomer A. S1 encompasses residues 11–20 in both monomers, S2 spans residues 31–38 in monomer A and residues 31–35 in monomer B. This structure, which lacks the salt bridge between Asp^{23} and Lys^{28}, has replaced the native intramolecular contacts between the strands S1 and S2 (Fig. 6 *b*, panels *AA* and *BB*) by nonnative intermolecular contacts between residues 34–40 of monomer A and residues 14–20 of monomer B (Fig. 6 *b*, panel *BA*).

Aβ_{40}-A21G in Fig. 5 *c* is also a four-stranded β-sheet with the strands S1 in parallel register, but the strands S2 are separated by 15 Å from each other and folded back against their strands S1. Strand S1 spans residues 13–19 and 13–16 in monomers A and B, whereas strand S2 covers residues 35–38 in monomer A and 34–35 in monomer B. The interface between the chains is essentially nonnative (Fig. 6 *c*, panels *AB* and *BA*), although the intramolecular intermolecular Phe^{19} and Met^{35} is preserved, and is characterized by a cluster of interactions between Met^{35}, and eight residues at positions 17, 19, 20, 23, 27, 28, and 31 (Fig. 6 *c*, panel *AA*).

The final topology of Aβ changes drastically with the presence of residues Ile^{41} and Ala^{42}. Aβ_{42} is essentially characterized by a seven-stranded β-sheet, although a short α-helix occurs at positions 22–26 in monomer A (Fig. 5 *d*). The strands cover residues 14–20, 26–27, 30–31, and 36–41 in monomer A and residues 10–20, 32–33, and 38–40 in monomer B. Two salt bridges are formed: one between Glu^{22} and Lys^{16} within monomer B and the other between Asp^{23} of monomer B and Lys^{28} of monomer A. Met^{35} of monomer A is in contact with Phe^{19} of both monomers. In contrast to Aβ_{42}, Aβ_{42}-A21G leads to a five-stranded β-sheet with mixed parallel and antiparallel strands (Fig. 5 *e*). Strands encompass residues 11–27 and 29–39 in monomer A, and residues 13–18, 25–33, and 39–42 in monomer B. The intramolecular salt bridge between Glu^{22} and Lys^{28} is only formed in monomer B, and Met^{35} is in contact with Phe^{19} and Phe^{20} of monomer A.

It is of interest to determine the native interactions and the structural features that are shared by all four Aβ species. We find that only the native intermolecular contact between

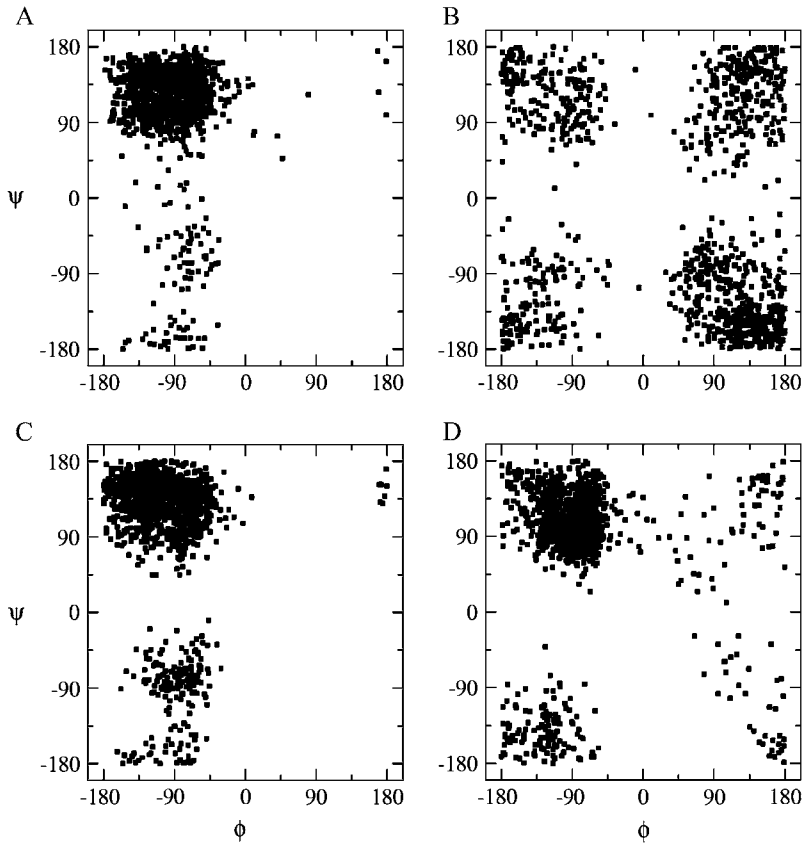

FIGURE 4 Ramachandran plot of residue 21. (*A*) $A\beta_{40}$, (*B*) $A\beta_{40}$-A21G, (*C*) $A\beta_{42}$, and (*D*) $A\beta_{42}$-A21G. Dihedral angles ϕ and ψ are reported using both monomers.

His^{14} residues is conserved in all species. All final Aβ dimers disrupt the interfaces between the strands S1 and S2, and between the strands of S2, but tend to preserve the interactions between the central hydrophobic clusters (CHC) spanning residues Leu^{17}-Ala^{21}, although the contacts observed are not conserved. For instance, the native intermolecular interaction between Phe^{19} residues is conserved in $A\beta_{40}$, $A\beta_{42}$, and its variant, but not in $A\beta_{40}$-A21G.

TABLE 2 Formation time percentage of intramolecular and intermolecular salt bridges between the residues Glu^{22} and Lys^{28} and between the residues Asp^{23} and Lys^{28}

	NMR†					
Interaction*	$A\beta_{40}$	$A\beta_{42}$	$A\beta_{40}$	$A\beta_{40}$-A21G	$A\beta_{42}$	$A\beta_{42}$-A21G
22^A-28^A	0	0	1.1	7.5	9.0	0
22^A-28^B	0	0	0	2.0	0	0
22^B-28^B	0	0	9.6	5.3	0	12.2
22^B-28^A	0	0	0	0	0.7	3.6
23^A-28^A	100	0	28.5	18.5	21.6	7.4
23^A-28^B	0	0	0	0.9	0	0.7
23^B-28^B	100	0	23.3	13.8	12.1	15.1
23^B-28^A	0	100	22.6	3.3	2.1	13.4

*Time percentage of formed salt bridge xx^X-yy^Y during the 10-ns simulations. In this notation, *xx* and *yy* refer to the amino-acid number and *X* and *Y* to the monomer number. Salt bridges are considered formed if the chosen atoms (described in the text) come within 4.2 Å.
†Refers to the 2002 $A\beta_{40}$ model (4) and the 2005 $A\beta_{42}$ model (6).

Comparison with in vitro and previous in silico experiments

Solution NMR studies of $A\beta_{10-35}$ (47), $A\beta_{1-40}$, and $A\beta_{1-42}$ (48) showed that CHC is the most structured region. Similarly, MD simulations of $A\beta_{10-35}$ in monomeric (49) and dimeric (24) forms showed that the CHC region is much less flexible than the rest of the protein. We find that this region, which is known to be essential for aggregation (50), is well conserved in wild-type $A\beta_{40}$ and $A\beta_{42}$, but not in their variants, strands S1 covering residues 13–16 and 13–18 in the monomers B of $A\beta_{40}$-A21G and $A\beta_{42}$-A21G, respectively.

The residues Ile^{41} and Ala^{42} are known to play a crucial role in Aβ oligomerization. Moritomo et al. (9) found that the $A\beta_{42}$ I41T and A42T mutants aggregate potently, and proposed that the hydrophobicity of the C-terminal two residues of $A\beta_{42}$ is not related to its aggregative ability, and that the C-terminal three residues adopt the β-sheet.

Hou et al. (48) measured $^1H_\alpha$, $^{13}C_\alpha$, and $^{13}C_\beta$ chemical shift indices of the $A\beta_{1-40}$ and $A\beta_{1-42}$ monomeric species and found that the C-terminus of $A\beta_{1-42}$ has a propensity for β-sheet structure, whereas that of $A\beta_{1-40}$ has not. Lazo et al. (31) coupled limited proteolysis and mass spectrometry and found that the residues Val^{39}-Ala^{42} are protease-resistant in $A\beta_{1-42}$, while the residues Val^{39}-Ala^{40} are not in $A\beta_{1-40}$. We find that the residues 41 and 42 have two major effects on the structure. Firstly, they favor the extension and formation of

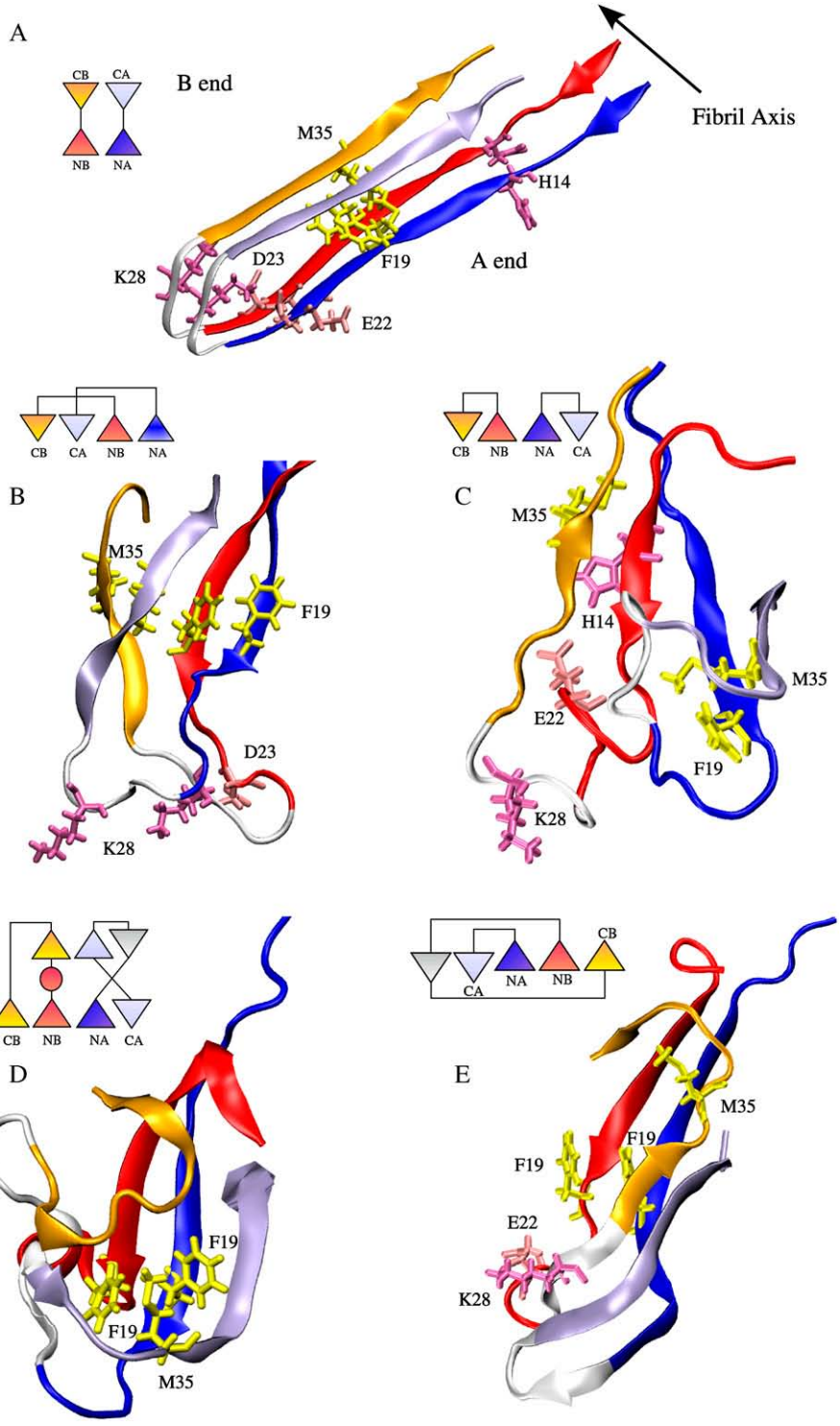

FIGURE 5 Final structures and topologies of Aβ dimers. (*A*) The initial dimer of Aβ_{40} used for the simulations, and the location of the residues His[14], Phe[19], Glu[22], Asp[23], Lys[28], and Met[35]. The center of the most populated clusters within 7.5–10 ns are shown for Aβ_{40} (*B*), Aβ_{40}-A21G (*C*), Aβ_{42} (*D*), and Aβ_{42}-A21G (*E*). The TOPS cartoon of each topology is also given and full explanation of the cartoons can be found at http://www3.ebi.ac.uk/tops/ExplainSummary.html. In brief, monomer A runs from NA to CA, and monomer B from NB and CB. Triangular and circular symbols represent the β-strands and α-helices, respectively. Triangles on the same horizontal row indicate hydrogen-bonding interactions between the strands. In all panels, residues 9–25 are in blue within monomer A and in red within monomer B; residues 26–30 are in white, and residues 31–40 (or 31–42) are in gray within monomer A and in orange within monomer B.

β-strand at position 39–42. Secondly, they disrupt the native interface between the chains and enhance the number of intramolecular interactions, irrespective of the amino acid at position 21. As seen in panels *AA* and *BB* of Fig. 6, *d* and *e*, both Aβ_{42} and Aβ_{42}-A21G species display two new domains (*encircled*) that are absent in the Aβ_{40} species: one involving residues 13–27 and 29–42 in monomer A, the other involving residues 10–17 and 37–42 in monomer B. In particular, Aβ_{42} and its mutant display de novo intramolecular interactions between (Ile[41], Ala[42]) and (His[14], Gln[15], Lys[16], Val[18], and Phe[19]). In addition, we see that Met[35] contacts Val[40] in Aβ_{42} and its A21G mutant, whereas Met[35] does not contact the C-terminal residues in Aβ_{40} and its A21G mutant. This difference in Met[35] contacts between the

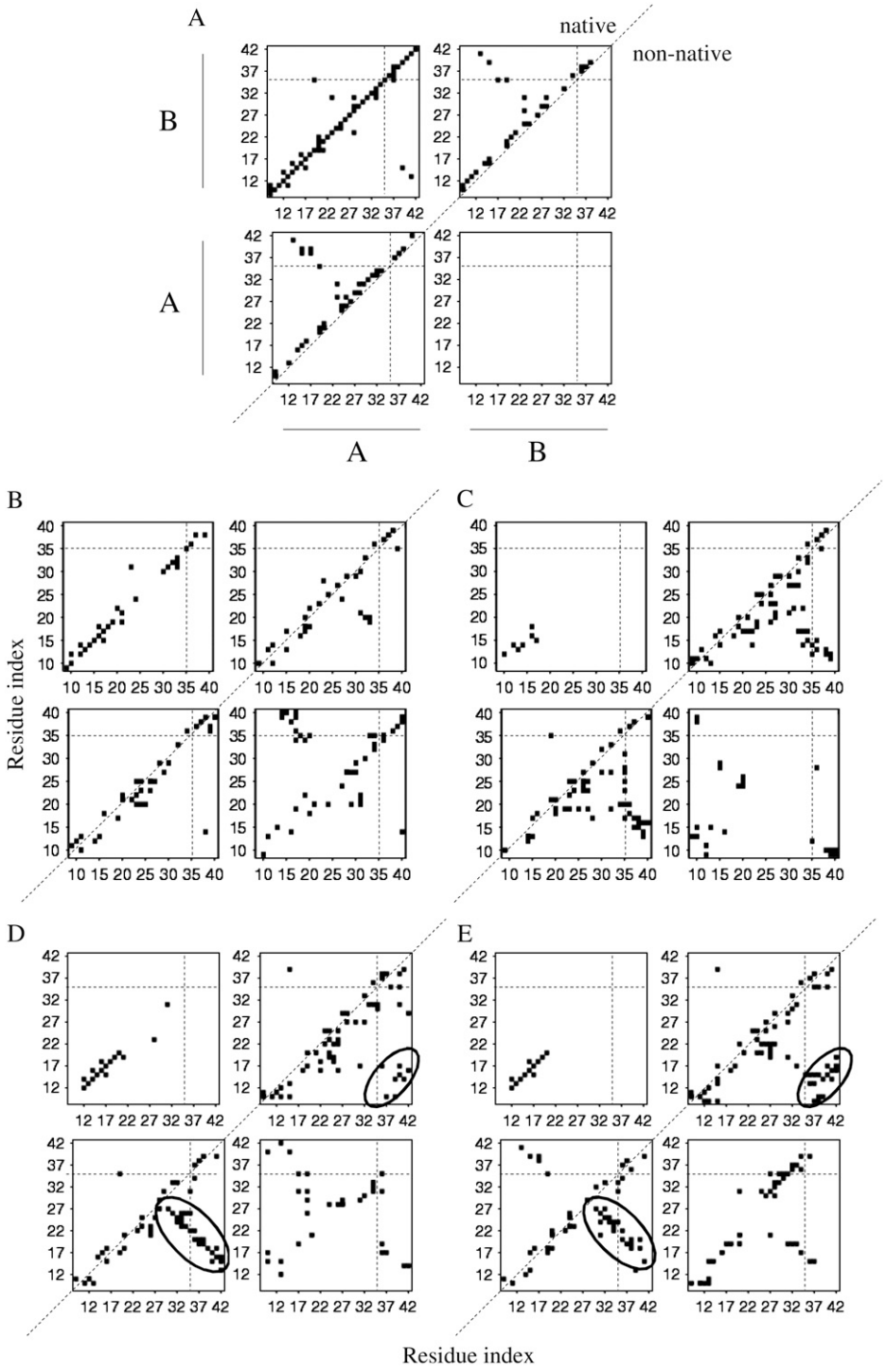

FIGURE 6 Sidechain-sidechain contact maps of Aβ dimers. (*A*) Initial $A\beta_{40}$, (*B*) final $A\beta_{40}$, (*C*) final $A\beta_{40}$-A21G, (*D*) final $A\beta_{42}$, and (*E*) final $A\beta_{42}$-A21G maps for the structures shown in Fig. 5. Each Aβ species is described by four panels: panels *AA* and *BB* show the intramolecular contacts within monomers A and B, respectively; panels *AB* and *BA* show the intermolecular interactions between monomers A and B, and between B and A, respectively. A diagonal dotted line is drawn to separate the native (*upper*) from nonnative (*lower*) interactions, and a vertical and horizontal dotted line indicates the position of the residue Met^{35}. The criteria used for defining a contact are described in Materials and Methods.

$A\beta_{40}$ and $A\beta_{42}$ species is made possible by the formation of a turn centered at Gly^{37}-Gly^{38} in $A\beta_{42}$, but not in $A\beta_{40}$ (see Fig. 3). Such a finding is fully consistent with DMD simulations of multimers (29) and MD simulations of a monomer (51).

Several studies have emphasized the importance of the intramolecular salt bridge between residues 23 and 28 in fibril formation (5,33). An engineered lactam bridge between Asp^{23} and Lys^{28} increases the $A\beta_{1-40}$ fibrillogenesis rate by three orders of magnitude (52). Solution NMR study and DMD simulations of the fragment $A\beta_{21-30}$ also suggested a possible mechanism for the effects of mutations at positions 22 and 23, based on a change of the populations of the salt bridges 23:28 and 22:28 (31,32). In contrast, the NMR fibril model of $A\beta_{17-42}$ points to an intermolecular salt bridge between residues 23 and 28. Our simulations provide strong

evidence of the existence of all these salt bridges in equilibrium, whose populations are determined by the presence of Ile^{41} and Ala^{42}, and the nature of the amino acid at position 21.

CONCLUSIONS

We have studied the impact of the point mutation A21G on the structure of Aβ dimers, by using a total of six unfolding molecular dynamics simulations at 400 K. All simulations of Aβ_{40}, Aβ_{42}, and their variants start from the conformation within the NMR 2002 fibril model of Aβ_{40}. Although this structure differs from the 2005 and 2006 models, it is a reasonable starting point because there is strong evidence that a unique structure does not exist, polymorphism likely reflecting multiples alternatives for the packing and interactions within the core of the fibril (33). In addition, we are only interested in the qualitative effect of Flemish mutation on the stability of different Aβ dimers and on the kinetics of assembly. Quantitative analysis is beyond the scope of this work for two reasons. The first reason is that a direct comparison between conformational distributions from experiment and simulation is difficult. Circular dichroism and NMR studies of low molecular weight Aβ, consisting of monomers and dimers in equilibrium with multimers as large as heptamers, give 60–80% of random coils, 10–20% of β-strand, and $<$10% of α-helix (53–55). We obtain a time-averaged β-percentage of 26% (Aβ_{42},Aβ_{40}-A21G), 35% (Aβ_{40}), and 40% (Aβ_{42}-A21G) excluding the first 5-ns and considering residues 1–8 disordered. Circular dichroism and NMR being averaging techniques, it is not possible to determine whether the β-signal originates from all Aβ species or whether some dimeric conformations with high (but not the highest) population exist with a richer β-composition. In addition, we cannot exclude the possibility that the simulations have not reached equilibrium yet. The second reason is that the effects of the GROMOS force field on the dynamics should be confirmed using other physically based force fields. The two main findings of this study can be summarized as follows.

Firstly, Aβ dimers are found in equilibrium between a wide range of topologies, ranging from four-stranded to seven-stranded β-sheets, with the strands S2 very mobile and the location of the strands S1 fluctuating between residues 11–20 (in Aβ_{40}) and residues 13–16 (in Aβ_{40}-A21G). This finding raises the question whether an unique inhibitor can block propagation of these structurally distinct dimers into protofibrils.

Secondly, the effect of A21G mutation on Aβ dimers is length-dependent and the structures and dynamics of Aβ_{42}-A21G cannot be extrapolated from those of Aβ_{40}-A21G, and vice versa. This is consistent with earlier experimental studies suggesting that substitutions at positions 22 and 23 produce different effects on Aβ assembly depending on whether they occur in Aβ_{40} or Aβ_{42} (56). Specifically, we find that the mutation A21G impacts Aβ dimers in three ways. A21G destabilizes the β-sheets and notably strands S2 in Aβ_{40}, but not in Aβ_{42}. A21G also increases, to a higher extent, the flexibility of the central hydrophobic cluster spanning residues 17–21 in Aβ_{40} than in Aβ_{42}, and affects, to various degrees, the populations of the intramolecular and intermolecular salt bridges involving Glu^{22}, Asp^{23}, and Lys^{28} in Aβ_{40} and Aβ_{42}. These three factors likely slow down the formation of higher-order species to direct further assembly into protofibril and could explain the reduced aggregation rate of Aβ fibrils containing the Flemish disease-causing mutation.

We thank R. Tycko for careful reading of the manuscript and for the PDB file of the 2002 Aβ_{40} fibril, and R. Riek for providing us with the coordinates of the Aβ_{42} fibril.

A.H. is supported by the Ministère de l'Education. P.D. thanks the CNRS and Université of Paris 7 for financial support and the Centre Informatique de l'Enseignement Supérieur and Institut du Développement et des Resources en Informatique Scientifique centers for providing computational support.

REFERENCES

1. Dobson, C. M. 2003. Protein folding and misfolding. *Nature*. 426:884–890.
2. Kang, J., H. G. Lemaire, A. Unterbeck, J. M. Salbaum, C. L. Masters, K. H. Grzeschik, G. Multhaup, K. Beyreuther, and B. Muller-Hill. 1987. The precursor of Alzheimer's disease amyloid A4 protein resembles a cell-surface receptor. *Nature*. 325:733–736.
3. Nelson, R., M. R. Sawaya, M. Balbirnie, A. Madsen, C. Riekel, R. Grothe, and D. Eisenberg. 2005. Structure of the cross-β spine of amyloid-like fibrils. *Nature*. 435:773–778.
4. Petkova, A. T., Y. Ishii, J. J. Balbach, O. N. Antzutkin, R. D. Leapman, F. Delaglio, and R. Tycko. 2002. A structural model for Alzheimer's β-amyloid fibrils based on experimental constraints from solid state NMR. *Proc. Natl. Acad. Sci. USA*. 99:16742–16747.
5. Petkova, A. T., W.-M. Yau, and R. Tycko. 2006. Experimental constraints on quaternary structure in Alzheimer's β-amyloid fibrils. *Biochemistry*. 45:498–512.
6. Luhrs, T., C. Ritter, M. Adrian, D. Riek-Loher, B. Bohrmann, H. Dobeli, D. Schubert, and R. Riek. 2005. 3D structure of Alzheimer's amyloid-β(1–42) fibrils. *Proc. Natl. Acad. Sci. USA*. 102:17342–17347.
7. Olofsson, A., A. E. Sauer-Eriksson, and A. Ohman. 2006. The solvent protection of Alzheimer amyloid-β-(1–42) fibrils as determined by solution NMR spectroscopy. *J. Biol. Chem.* 281:477–483.
8. Williams, A. D., S. Shivaprasad, and R. Wetzel. 2006. Alanine scanning mutagenesis of Aβ (1–40) amyloid fibril stability. *J. Mol. Biol.* 357:1283–1294.
9. Morimoto, A., K. Irie, K. Murakami, Y. Masuda, H. Ohigashi, M. Nagao, H. Fukuda, T. Shimizu, and T. Shirasawa. 2004. Analysis of the secondary structure of β-amyloid (Aβ-42) fibrils by systematic proline replacement. *J. Biol. Chem.* 279:52781–52788.
10. Bitan, G., M. D. Kirkitadze, A. Lomakin, S. S. Vollers, G. B. Benedek, and D. B. Teplow. 2003. Amyloid β-protein (Aβ) assembly: Aβ-40 and Aβ-42 oligomerize through distinct pathways. *Proc. Natl. Acad. Sci. USA*. 100:330–335.
11. Hendriks, L., C. M. van Duijn, P. Cras, M. Cruts, W. V. Hul, F. van Harskamp, A. Warren, M. G. McInnis, S. E. Antonarakis, and J. J. Martin. 1992. Presenile dementia and cerebral haemorrhage linked to a mutation at codon 692 of the β-amyloid precursor protein gene. *Nat. Genet.* 1:218–221.
12. Levy, E., M. D. Carman, I. J. Fernandez-Madrid, M. D. Power, I. Lieberburg, S. G. van Duinen, G. T. Bots, W. Luyendijk, and B. Frangione. 1990. Mutation of the Alzheimer's disease amyloid gene in hereditary cerebral hemorrhage, Dutch type. *Science*. 248:1124–1126.

13. Broeckhoven, C. V., J. Haan, E. Bakker, J. A. Hardy, W. V. Hul, A. Wehnert, M. V.-V. der Vlis, and R. A. Roos. 1990. Amyloid β-protein precursor gene and hereditary cerebral hemorrhage with amyloidosis (Dutch). *Science.* 248:1120–1122.

14. Rossi, G., G. Macchi, M. Porro, G. Giaccone, M. Bugiani, E. Scarpini, G. Scarlato, G. E. Molini, F. Sasanelli, O. Bugiani, and F. Tagliavini. 1998. Fatal familial insomnia: genetic, neuropathologic, and biochemical study of a patient from a new Italian kindred. *Neurology.* 50:688–692.

15. Nilsberth, C., A. Westlind-Danielsson, C. B. Eckman, M. M. Condron, K. Axelman, C. Forsell, C. Stenh, J. Luthman, D. B. Teplow, S. G. Younkin, J. Naslund, and L. Lannfelt. 2001. The ''Arctic'' APP mutation (E693G) causes Alzheimer's disease by enhanced Aβ protofibril formation. *Nat. Neurosci.* 4:887–893.

16. Grabowski, T. J., H. S. Cho, J. P. Vonsattel, G. W. Rebeck, and S. M. Greenberg. 2001. Novel amyloid precursor protein mutation in an Iowa family with dementia and severe cerebral amyloid angiopathy. *Ann. Neurol.* 49:697–705.

17. Murakami, K., K. Irie, A. Morimoto, H. Ohigashi, M. Shindo, M. Nagao, T. Shimizu, and T. Shirasawa. 2002. Synthesis, aggregation, neurotoxicity, and secondary structure of various A β 1–42 mutants of familial Alzheimer's disease at positions 21–23. *Biochem. Biophys. Res. Commun.* 294:5–10.

18. Murakami, K., K. Irie, A. Morimoto, H. Ohigashi, M. Shindo, M. Nagao, T. Shimizu, and T. Shirasawa. 2003. Neurotoxicity and physicochemical properties of Aβ mutant peptides from cerebral amyloid angiopathy: implication for the pathogenesis of cerebral amyloid angiopathy and Alzheimer's disease. *J. Biol. Chem.* 278:46179–46187.

19. Roher, A. E., M. O. Chaney, Y. M. Kuo, S. D. Webster, W. B. Stine, L. J. Haverkamp, A. S. Woods, R. J. Cotter, J. M. Tuohy, G. A. Krafft, B. S. Bonnell, and M. R. Emmerling. 1996. Morphology and toxicity of Aβ-(1–42) dimer derived from neuritic and vascular amyloid deposits of Alzheimer's disease. *J. Biol. Chem.* 271:20631–20635.

20. Cleary, J. P., D. M. Walsh, J. J. Hofmeister, G. M. Shankar, M. A. Kuskowski, D. J. Selkoe, and K. H. Ashe. 2005. Natural oligomers of the amyloid-β protein specifically disrupt cognitive function. *Nat. Neurosci.* 8:79–84.

21. Soreghan, B., J. Kosmoski, and C. Glabe. 1994. Surfactant properties of Alzheimer's Aβ peptides and the mechanism of amyloid aggregation. *J. Biol. Chem.* 269:28551–28554.

22. Garzon-Rodriguez, W., M. Sepulveda-Becerra, S. Milton, and C. G. Glabe. 1997. Soluble amyloid Aβ-(1–40) exists as a stable dimer at low concentrations. *J. Biol. Chem.* 272:21037–21044.

23. Garzon-Rodriguez, W., A. Vega, M. Sepulveda-Becerra, S. Milton, D. A. Johnson, A. K. Yatsimirsky, and C. G. Glabe. 2000. A conformation change in the carboxyl terminus of Alzheimer's Aβ (1–40) accompanies the transition from dimer to fibril as revealed by fluorescence quenching analysis. *J. Biol. Chem.* 275:22645–22649.

24. Tarus, B., J. E. Straub, and D. Thirumalai. 2005. Probing the initial stage of aggregation of the Aβ (10–35)-protein: assessing the propensity for peptide dimerization. *J. Mol. Biol.* 345:1141–1156.

25. Tao Guo, J., R. Wetzel, and Y. Xu. 2004. Molecular modeling of the core of Aβ amyloid fibrils. *Proteins.* 57:357–364.

26. Ma, B., and R. Nussinov. 2002. Stabilities and conformations of Alzheimer's β-amyloid peptide oligomers (Aβ 16–22, Aβ 16–35, and Aβ 10–35): sequence effects. *Proc. Natl. Acad. Sci. USA.* 99:14126–14131.

27. Buchete, N.-V., R. Tycko, and G. Hummer. 2005. Molecular dynamics simulations of Alzheimer's β-amyloid protofilaments. *J. Mol. Biol.* 353:804–821.

28. Urbanc, B., L. Cruz, F. Ding, D. Sammond, S. Khare, S. V. Buldyrev, H. E. Stanley, and N. V. Dokholyan. 2004. Molecular dynamics simulation of amyloid β-dimer formation. *Biophys. J.* 87:2310–2321.

29. Urbanc, B., L. Cruz, S. Yun, S. V. Buldyrev, G. Bitan, D. B. Teplow, and H. E. Stanley. 2004. In silico study of amyloid β-protein folding and oligomerization. *Proc. Natl. Acad. Sci. USA.* 101:17345–17350.

30. Paravastu, A. K., A. T. Petkova, and R. Tycko. 2006. Polymorphic fibril formation by residues 10–40 of the Alzheimer's β-amyloid peptide. *Biophys. J.*

31. Lazo, N. D., M. A. Grant, M. C. Condron, A. C. Rigby, and D. B. Teplow. 2005. On the nucleation of amyloid β-protein monomer folding. *Protein Sci.* 14:1581–1596.

32. Borreguero, J. M., B. Urbanc, N. D. Lazo, S. V. Buldyrev, D. B. Teplow, and H. E. Stanley. 2005. Folding events in the 21–30 region of amyloid β-protein (Aβ) studied in silico. *Proc. Natl. Acad. Sci. USA.* 102:6015–6020.

33. Petkova, A. T., R. D. Leapman, Z. Guo, W.-M. Yau, M. P. Mattson, and R. Tycko. 2005. Self-propagating, molecular-level polymorphism in Alzheimer's β-amyloid fibrils. *Science.* 307:262–265.

34. Spoel, D. V. D., E. Lindahl, B. Hess, G. Groenhof, A. E. Mark, and H. J. C. Berendsen. 2005. GROMACS: fast, flexible, and free. *J. Comput. Chem.* 26:1701–1718.

35. Guex, N., and M. C. Peitsch. 1997. SWISS-MODEL and the Swiss-PdbViewer: an environment for comparative protein modeling. *Electrophoresis.* 18:2714–2723.

36. Walser, R., A. E. Mark, and W. F. van Gunsteren. 2000. On the temperature and pressure dependence of a range of properties of a type of water model commonly used in high-temperature protein unfolding simulations. *Biophys. J.* 78:2752–2760.

37. Dinner, A. R., and M. Karplus. 1999. Is protein unfolding the reverse of protein folding? A lattice simulation analysis. *J. Mol. Biol.* 292:403–419.

38. Klimov, D. K., and D. Thirumalai. 2005. Symmetric connectivity of secondary structure elements enhances the diversity of folding pathways. *J. Mol. Biol.* 353:1171–1186.

39. Frishman, D., and P. Argos. 1995. Knowledge-based protein secondary structure assignment. *Proteins.* 23:566–579.

40. Day, R., B. J. Bennion, S. Ham, and V. Daggett. 2002. Increasing temperature accelerates protein unfolding without changing the pathway of unfolding. *J. Mol. Biol.* 322:189–203.

41. Humphrey, W., A. Dalke, and K. Schulten. 1996. VMD: visual molecular dynamics. *J. Mol. Graph.* 14:27–38.

42. Dima, R. I., and D. Thirumalai. 2002. Exploring protein aggregation and self-propagation using lattice models: phase diagram and kinetics. *Protein Sci.* 11:1036–1049.

43. Santini, S., G. Wei, N. Mousseau, and P. Derreumaux. 2004. Pathway complexity of Alzheimer's β-amyloid Aβ-16–22 peptide assembly. *Structure.* 12:1245–1255.

44. Lee, B., and F. M. Richards. 1971. The interpretation of protein structures: estimation of static accessibility. *J. Mol. Biol.* 55:379–400.

45. Ghosh, T., S. Garde, and A. E. Garcia. 2003. Role of backbone hydration and salt-bridge formation in stability of α-helix in solution. *Biophys. J.* 85:3187–3193.

46. Gilbert, D., D. Westhead, N. Nagano, and J. Thornton. 1999. Motif-based searching in TOPS protein topology databases. *Bioinformatics.* 15:317–326.

47. Zhang, S., K. Iwata, M. J. Lachenmann, J. W. Peng, S. Li, E. R. Stimson, Y. Lu, A. M. Felix, J. E. Maggio, and J. P. Lee. 2000. The Alzheimer's peptide Aβ adopts a collapsed coil structure in water. *J. Struct. Biol.* 130:130–141.

48. Hou, L., H. Shao, Y. Zhang, H. Li, N. K. Menon, E. B. Neuhaus, J. M. Brewer, I.-J. L. Byeon, D. G. Ray, M. P. Vitek, T. Iwashita, R. A. Makula, A. B. Przybyla, and M. G. Zagorski. 2004. Solution NMR studies of the Aβ (1–40) and Aβ (1–42) peptides establish that the Met^{35} oxidation state affects the mechanism of amyloid formation. *J. Am. Chem. Soc.* 126:1992–2005.

49. Massi, F., J. W. Peng, J. P. Lee, and J. E. Straub. 2001. Simulation study of the structure and dynamics of the Alzheimer's amyloid peptide congener in solution. *Biophys. J.* 80:31–44.

50. Narayanan, S., and B. Reif. 2005. Characterization of chemical exchange between soluble and aggregated states of β-amyloid by solution-state NMR upon variation of salt conditions. *Biochemistry.* 44:1444–1452.

51. Flock, D., S. Colacino, G. Colombo, and A. D. Nola. 2006. Misfolding of the amyloid β-protein: a molecular dynamics study. *Proteins.* 62:183–192.

52. Sciarretta, K. L., D. J. Gordon, A. T. Petkova, R. Tycko, and S. C. Meredith. 2005. Aβ40-Lactam(D23/K28) models a conformation highly favorable for nucleation of amyloid. *Biochemistry.* 44:6003–6014.

53. Bitan, G., S. S. Vollers, and D. B. Teplow. 2003. Elucidation of primary structure elements controlling early amyloid β-protein oligomerization. *J. Biol. Chem.* 278:34882–34889.

54. Huang, T. H., D. S. Yang, N. P. Plaskos, S. Go, C. M. Yip, P. E. Fraser, and A. Chakrabartty. 2000. Structural studies of soluble oligomers of the Alzheimer β-amyloid peptide. *J. Mol. Biol.* 297:73–87.

55. Walsh, D. M., D. M. Hartley, Y. Kusumoto, Y. Fezoui, M. M. Condron, A. Lomakin, G. B. Benedek, D. J. Selkoe, and D. B. Teplow. 1999. Amyloid β-protein fibrillogenesis. Structure and biological activity of protofibrillar intermediates. *J. Biol. Chem.* 274:25945–25952.

56. Kirkitadze, M. D., M. M. Condron, and D. B. Teplow. 2001. Identification and characterization of key kinetic intermediates in amyloid β-protein fibrillogenesis. *J. Mol. Biol.* 312:1103–1119.